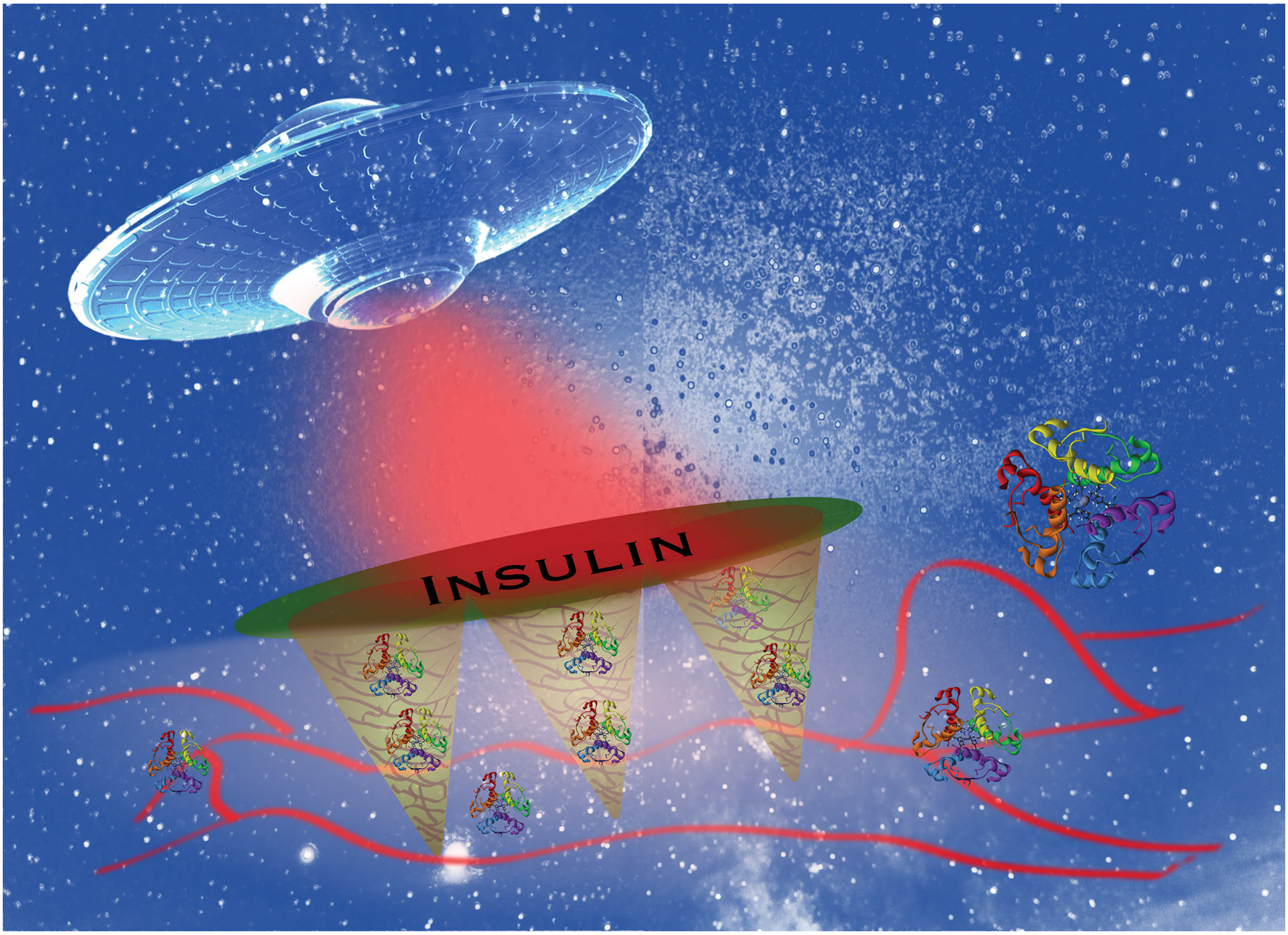

Showcasing research from Professor Szunerits, IEMN, University of Lille, France and Dr Severine Vignoud, CEA Grenoble, France.

Innovative transdermal delivery of insulin using gelatin methacrylate-based microneedle patches in mice and mini-pigs

Painless and controlled on-demand insulin delivery is achieved by using near infra-red (NIR) light activatable non-dissolving microneedles. The microneedles are formed by cross-linking gelatin methacrylate with polyethylene glycol diacrylate (PEGDA) in the presence of MoS_2 nanosheets as the photothermal component. Transdermal administration of insulin loaded microneedle arrays reduces blood glucose levels in C57BL/6 mice and mini-pigs comparable to subcutaneously injected insulin.

As featured in:


Nanoscale Horizons

See Severine Vignoud, Sabine Szunerits *et al.*, *Nanoscale Horiz.*, 2022, **7**, 174.

ROYAL SOCIETY OF CHEMISTRY

rsc.li/nanoscale-horizons

Registered charity number: 207890

Nanoscale
Horizons

Cite this: *Nanoscale Horiz.*, 2022, 7, 174

Received 14th November 2021, Accepted 22nd December 2021

DOI: 10.1039/d1nh00596k

rsc.li/nanoscale-horizons

Innovative transdermal delivery of insulin using gelatin methacrylate-based microneedle patches in mice and mini-pigs†

Bilal Demir,[abc] Lea Rosselle,[c] Anna Voronova,[c] Quentin Pagneux,[c] Audrey Quenon,[d] Valery Gmyr,[d] Dorothee Jary,[b] Nathalie Hennuyer,[e] Bart Staels,[e] Thomas Hubert,[d] Amar Abderrahmani,[c] Valerie Plaisance,[c] Valerie Pawlowski,[c] Rabah Boukherroub,[c] Severine Vignoud*[b] and Sabine Szunerits *[c]

Painless and controlled on-demand drug delivery is the ultimate goal for the management of various chronic diseases, including diabetes. To achieve this purpose, microneedle patches are gaining increased attention. While degradable microneedle (MN) arrays are widely employed, the use of non-dissolving MN patches remains a challenge to overcome. In this study, we demonstrate that cross-linking gelatin methacrylate with polyethylene glycol diacrylate (PEGDA) is potent for engineering non-dissolving MN arrays. Incorporation of MoS_2 nanosheets as a photothermal component into MN hydrogels results in MNs featuring on-demand release properties. An optimized MoS_2-MN array patch formed using a hydrogel solution containing 500 $\mu g\ mL^{-1}$ of MoS_2 and photochemically crosslinked for 5 min shows required mechanical behavior under a normal compressive load to penetrate the stratum corneum of mice or pig skin and allows the delivery of macromolecular therapeutics such as insulin upon swelling. Using *ex vivo* and *in vivo* models, we show that the MoS_2-MN patches can be used for loading and releasing insulin for therapeutic purposes. Indeed, transdermal administration of insulin loaded into MoS_2-MN patches reduces blood glucose levels in C57BL/6 mice and mini-pigs comparably to subcutaneously injected insulin. We believe that this on-demand delivery system might alter the current insulin therapies and might be a potential approach for delivery of other proteins.

New concepts

We developed a new concept based on photothermally active non-dissolving microneedle arrays for the transdermal delivery of drugs such as insulin. This is different from other microneedle-based drug delivery approaches as it involves non-dissolving hydrogel microneedles where drug release is initiated photothermally rather than drug delivery *via* dissolving microneedles. By using *in vitro* and two *in vivo* experiments, using mice and pigs, we studied the efficiency of the designed insulin delivery patch.

1. Introduction

Transdermal drug delivery systems, as non-invasive and painless drug delivery alternatives to intravenous and intramuscular drug injection, have attracted much research attention.[1–3] Microneedle-based technologies have, in particular, opened up promising avenues to overcome the barrier of the skin's stratum corneum for larger therapeutic agents such as proteins and peptides.[4–7] Unfortunately, the strength of the needles for piercing the stratum corneum, the biocompatibility with minimal side effects and the ability of the needles to release drugs on demand remain the technical challenges to overcome for implementing microneedle-based technologies in clinics. A large variety of microneedle arrays (MNs) have been manufactured over the last 20 years. They can be divided into polymeric,[7–15] silk fibroin,[5,16–19] and hydrogel-based microneedles.[20–25] So far, next to hollow microneedles,[26] biodegradable systems[18,25] as well as swelling microneedles[21] are engineered for improving the delivery of therapeutics over a prolonged time.

Drug delivery using non-dissolving systems has the advantage over biodegradable systems that they are reusable. Often the amount of released drug is limited. Drug release upon an external stimulus is one way to overcome these limitations.[27] To this end, photothermally-active graphene oxide (GO) was integrated into dissolvable polymeric microneedles, but to reinforce the scaffold rather than providing it with a stimuli-responsive matrix. Photothermally-controlled

---

[a] *CEA-TECH Region, Department Hauts-de-France, 165 Avenue de Bretagne, Lille 59000, France. E-mail: severine.vignoud@cea.fr*
[b] *LETI-DTBS, CEA, 17 rue des Martyrs, Grenoble 38054, France. E-mail: sabine.szunerits@univ-lille.fr*
[c] *Univ. Lille, CNRS, Centrale Lille, Univ. Polytechnique Hauts-de-France, UMR 8520 – IEMN, Lille F-59000, France*
[d] *Univ. Lille, CHU Lille, Inserm, European Genomic Institute of Diabetes (EGID), Institut Pasteur de Lille, UMR 1190, Lille F-59000, France*
[e] *Univ. Lille, Inserm, CHU Lille, Institut Pasteur de Lille, U1011 – EGID, Lille F-59000, France*

† Electronic supplementary information (ESI) available. See DOI: 10.1039/d1nh00596k

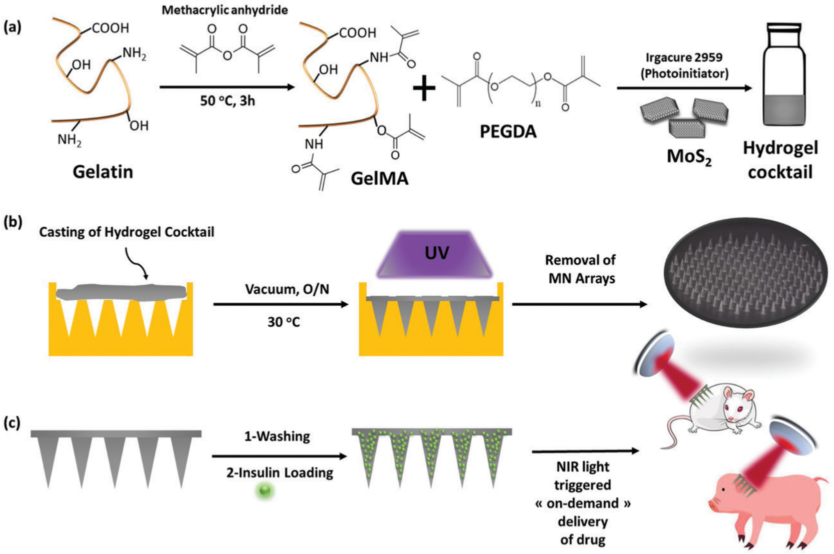

Fig. 1 Photothermal activatable MoS_2 loaded microneedles: (a) fabrication of a MoS_2-loaded hydrogel cocktail (2 mL containing 1 mg MoS_2) based on gelatin methacrylate (GelMA) and polyethylene glycol diacrylate (PEGDA) as hydrogel components. (b) Casting of hydrogel cocktail (300 μL) onto a microneedle mold and formation of the MoS_2 loaded microneedle array. (c) Loading of insulin into MoS_2-MNs and near-infrared light (NIR) triggered on-demand delivery to control the glycemic level in mice and minipigs.

release of rosiglitazone from melamine-modified microneedles has been proposed by Peng *et al*. using soluble MNs.[28] Fabrication of separable microneedles based on poly(vinyl alcohol)/sucrose with Prussian blue nanoparticles (PB NPs) as a photothermal agent and coated with lauric acid as phase transition coating for NIR-triggered transdermal delivery of metformin to diabetic rats has been the focus of the work by Liu *et al.*[29] Hardy *et al.* proposed the one and only "on-demand" microneedle-based drug delivery system.[24] It is based on the light-responsive 3,5-dimethoxybenzoin conjugate integrated into the microneedle gel for ibuprofen delivery upon an optical trigger.[24]

We found that many of these challenges can be addressed by the application of microneedles prepared from gelatin methacrylate (GelMA) crosslinked with polyethylene glycol diacrylate (PEGDA) (Fig. 1). GelMA is a hydrogel that has gained popularity recently as a photo-cross linkable biomaterial for tissue engineering applications[25,30] as well as for the sustained release of proteins.[31] In this work, we opted for the integration of molybdenum sulfide nanosheets (MoS_2 NSs) as a photothermal material.[32–34] Microneedles modified with MoS_2 have been reported earlier, although the topic was related to sensors.[35,36] While two-dimensional (2D) materials such as graphene oxide (GO)[37] and reduced graphene oxide (rGO)[38–42] have been successfully integrated into various hydrogels and fiber mats, we assessed the suitability of MoS_2 as a photothermal component in the MN delivery system. MoS_2, a layered semiconductor with a narrow band gap (1.2 eV for multilayer MoS_2), exhibits a strong near-infrared (NIR) optical absorption and is well-adapted for biomedical applications where NIR photothermal activity and chemical stability are required.[33] In contrast to peptide and protein adsorption on GO and rGO nanosheets, where H-bonding, π–π stacking and/or electrostatic interactions are dominating, molecular dynamics simulations validated that the aromatic residues of peptides and proteins do interact less strongly with MoS_2 nanosheets.[43] Therefore, the release of therapeutic peptides such as insulin should be favored under these conditions.

It could be indeed demonstrated in C57BL/6 mice and mini-pigs that insulin was efficiently released from such microneedle hydrogels while retaining its biological efficacy. In the two *in vivo* models, we observed an improvement in the transdermal bioavailability of insulin with excellent transdermal delivery.

2 Results and discussion

2.1. Fabrication of MoS_2 loaded microneedles based on GelMA and PEGDA hydrogels

Gelatin methacrylate (GelMA) hydrogels are formed when methacrylic anhydride reacts with the primary amine groups of gelatin at 50 °C (Fig. 1). The formed GelMA can be cross-linked under UV irradiation in the presence of an appropriate photoinitiator, which, upon UV light absorption, generated free radicals that subsequently induced GelMA polymerization. The critical factors influencing the final physicochemical properties of GelMA hydrogels are, next to the degree of gelation functionalization, the parameters of photo-crosslinking such as exposure time and UV intensity. In this study, GelMA was mixed with polyethylene glycol diacrylate (PEGDA), a commercially available hydrogel precursor with equal photopolymerization properties like GelMA, and MoS_2 to obtain a hydrogel cocktail for the fabrication of microneedles (Fig. 1). Owing to its polyethylene glycol (PEG) units, PEGDA provides an additional hydrophilic environment necessary for preserving the biological activity of many biomolecules, as lately shown by some of us using insulin.[42] In addition, GelMA-only microneedles are mechanically

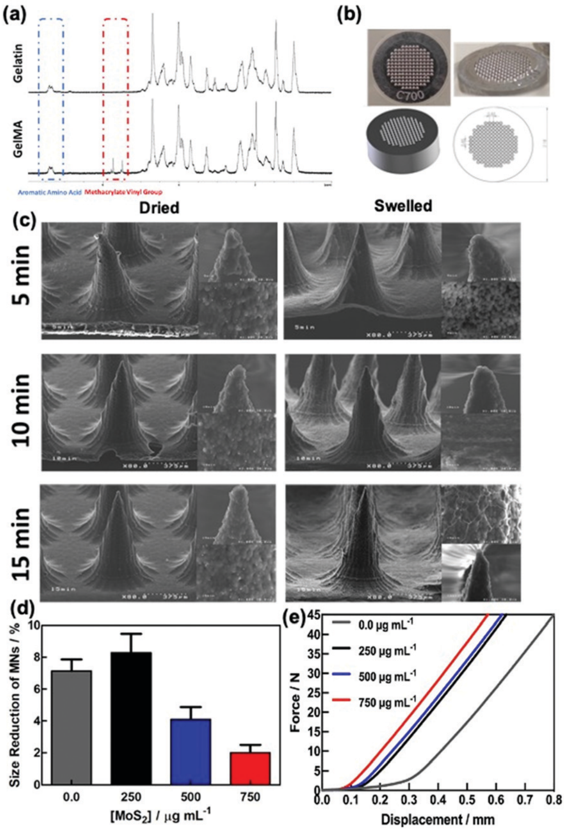

Fig. 2 Morphological characterization of MoS_2-MNs: (a) ^{1}H NMR of gelatin before and after methacrylation into GelMA. (b) Photographs of MN aluminum master molds from different perspectives. (c) SEM images of the MoS_2 loaded MN array using 300 μL of a hydrogel cocktail of GelMA : PEDGMA (20 : 10) (2 mL) and 1.0 mg MoS_2, polymerized using different UV irradiation times. (d) Influence of MoS_2 content (250, 500 and 750 μg mL^{-1}) in the hydrogel cocktail on the mechanical strength of MN hydrogel arrays. (e) Force–displacement curves recorded for GelMA : PEDGMA (20 : 10) hydrogel MNs without and with increasing MoS_2 content (250, 500 and 750 μg mL^{-1}) in the polymerization mixture.

fragile and addition of PEGDA gives the microneedle structures suitable elasticity for further applications.[44] The methacrylation of gelatin into GelMA was validated by ^{1}H NMR (Fig. 2a) by comparing to native gelatin. The signals at δ = 5.4 and 5.7 ppm correspond to the protons of the methacrylate vinyl group of methacrylic anhydride. The degree of methacrylation was calculated to be 89.4 ± 1.1% corresponding to 0.297 mmol g^{-1} of gelatin using trimethylsilylpropanoic acid (TMSP) as an internal standard.

The microneedles investigated in this work were prepared through micro-molding, an easy and cost-effective approach for hydrogel-based microneedle formation. Using a male master template array, prepared through 3D printing poly(dimethylsiloxane) (PDMS) (Fig. 2b), a female mold was obtained with a circular design incorporating 137 conical microneedles with a base of 400 μm, needles of 700 μm in height, and a needle center-to-center spacing of 850 μm (Fig. 2b).

It has been reported that upon increasing the GelMA concentration, the mechanical strength was enhanced,[30] while the swelling[30] as well as the size of the pores[45] decreased.

Different ratios of GelMA : PEGDA (20 : 5, 20 : 7.5 and 20 : 10) hydrogel cocktails were investigated for the formation of MoS_2-loaded MN patches and their swelling behavior. Indeed, a recent study on GelMA : PEGDA hydrogels showed that PEGDA addition (> 5% w/v) strengthened the hydrogel network in the presence of a 0.1% w/v photoinitiator.[44] The results support that a ratio of GelMA : PEGDA (20 : 10) with 0.5% w/v photoinitiator and 5 min of UV irradiation are well-suited for complete crosslinking. Fig. S1a (ESI†) illustrates the swelled morphologies after immersion for 24 h in water of the three MN patch formulations with increasing PEGDA amount, while keeping the MoS_2 amount at 500 μg mL^{-1} in the hydrogel cocktail. Apart from the MNs formed using a GelMA : PEGDA ratio of 20 : 10 that has a stable form in the swollen state, patches obtained using GelMA : PEGDA ratios of 20 : 5 and 20 : 7.5 were structurally fragile when swollen, brittle and/or broken after redrying. Hence, we opted for a hydrogel-based microneedle array based on GelMA mixed with polyethylene glycol diacrylate (PEGDA) in a weight ratio of 20 : 10, which is proven to be most suitable due to the good microneedle form (Fig. S1b, ESI†).

The UV irradiation time also has a significant effect on the mechanical performance of the needles. Fig. 2c shows the SEM images of the MoS_2-MN array formed using 300 μL of a hydrogel cocktail of GelMA : PEDGMA (20 : 10) (2 mL) and 1.0 mg of MoS_2 for different UV cross-linking times (5, 10 and 15 min) in the dried and swelled states. Each microneedle is conical in shape with a 5–10 μm radius of curvature at the tip depending on the crosslinking time and around 390 ± 6 μm at the base and 650 ± 21 μm in height. The dimensions of the needles were similar to the features of the male molds. The viscosity of gelatin and water evaporation during filling the needles might be affected by a small change in height values. Magnification of the tip of the MN shows a porous granulate structure, in particular, for the MNs formed upon 15 min irradiation. The presence of MoS_2 has a favorable effect on the morphology of the MNs and stiffens the hydrogel structures.

The mechanical properties of the MoS_2-MN arrays were investigated by changing the amount of MoS_2 used during MN production (Fig. 2d). Compression tests before and after imaging of the needles were performed. The observed size reduction, calculated before and after compression, correlates well with the relative force–displacement curves obtained by compression tests using a texturometer (Fig. 2e). From these experiments, it could be concluded that increasing the amount of MoS_2 used for MN fabrication results in a stronger force demand and enough to pierce the stratum corneum.

The swelling and biodegradability characteristics of MoS_2-MNs were assessed for different UV irradiation times (5, 10 and 15 min) applied during the fabrication process (Fig. S2a, ESI†). Samples formed using the irradiation times of 10 and 15 min when submerged into PBS at 32 °C revealed similar swelling properties after 24 h. In addition, a biodegradability test was performed in the presence of collagenase II in PBS at 32 °C to understand the properties of MoS_2-MN patches. Fig. S2b (ESI†) demonstrates that there was no difference among the three MN

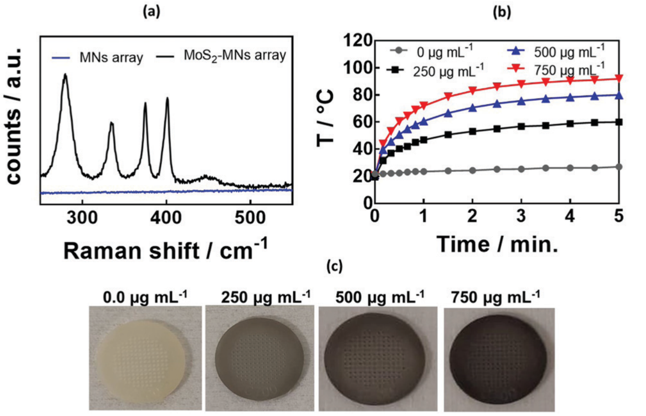

Fig. 3 Characterization of the MoS_2-MN array formed from a GelMA : PEDGMA (20 : 10) cocktail using different amounts of MoS_2: (a) Raman spectrum of the GelMA : PEDGMA hydrogel loaded with 500 μg mL^{-1} of MoS_2. (b) Photothermal heating properties of the MoS_2-MN array under irradiation with a laser at 980 nm (1.0 W cm^{-2}) as a function of MoS_2 amount in the hydrogel cocktail. (c) Photographic images of the MNs with increasing amounts of incorporated MoS_2.

patches prepared using different UV irradiation times thanks to the highly-crosslinked hydrogel structure achieved upon the addition of PEGDA.[46,47]

The presence of MoS_2 was evidenced from the Raman spectrum of the GelMA : PEDGMA (20 : 10) hydrogel MNs without and with increasing amounts of MoS_2 (Fig. 3a). At lower wavenumbers, the characteristic bands due to MoS_2 are visible at 286 cm^{-1} ($E_g{}^1$), 383 cm^{-1} ($E_{2g}{}^1$), 404 cm^{-1} (A_{1g} mode), and 450 cm^{-1} (2LA(M) mode). The band at 652 cm^{-1} is believed to be due to A_{1g} (M) + LA(M).[48]

The incorporation of MoS_2 into the GelMA : PEDGMA (20 : 10) hydrogel MNs resulted in rapid light to heat conversion (Fig. 3b). Indeed, MoS_2 exhibits absorption bands in the UV/vis as well as in the NIR (Fig. S3, ESI†) adapted for photothermal heating.[49] The photothermal heating was significantly larger when compared to previously reported PEGDMA-rGO hydrogels, reaching around 70 °C for 800 μg mL^{-1} of rGO using a laser density of 0.7 W cm^{-1}.[42] The photothermal effect correlated well with the color change upon MoS_2 loading onto the MNs (Fig. 3c). As expected, the higher the amount of MoS_2 incorporated in the hydrogel, the higher the temperature reached.

2.2. Biophysical properties of the MoS_2-MN patch

Before deploying the microneedle patches for *in vivo* insulin delivery, we investigated the physical properties such as mechanical strength for penetration of dermal tissue. The microneedle array formed using 500 μg mL^{-1} of MoS_2 possessed sufficient mechanical strength to penetrate the mouse skin (Fig. 4a) under compression (Fig. 4b) without causing damage to the microneedles. The SEM images indicated that the microneedles maintained their conical shape and sharp tips after removal from the mouse skin (Fig. 4c and d). Hematoxylin and eosin (H&E) staining of the mouse skin tissue further confirmed that the microneedles had penetrated the stratum corneum and perforated into the epidermal layer (Fig. 4e), with cellular infiltration indicated by white arrows.[50]

2.3. *In vitro* characterization of the insulin-loaded MoS_2-MN patch

The loading capacity of the MoS_2-MN patch for insulin was investigated by keeping the patch immersed in 100 μg mL^{-1} of insulin at 4 °C for 8 h (Fig. 5a). The entrapment efficiency, determined by HPLC from the insulin remaining in the solution,[51] was as high as 80 ± 2% (80 μg of insulin), which correlates to 2.3 IU for hydrogels formed using 5 min UV irradiation. Generally, to correct the high concentrations of blood sugar in humans, 0.3–1.0 IU kg^{-1} insulin is needed to decrease the blood glucose by 50 mg dL^{-1}.

Passive release of insulin was investigated by immersing the MoS_2-MN patches, in PBS at 37 °C (body temperature) for 12 h. Not more than 1 μg of insulin could be detected from the 80 μg loaded into the gel, indicating that passive release was restricted.

In a control experiment, hydrogels without MoS_2 were loaded with insulin. Crosslinking parameter-dependent insulin loading (Fig. S4a, ESI†) and release (Fig. S4b, ESI†) efficiencies were observed. This underlines the importance of MoS_2 not only to increase the mechanical strength of the MNs, but also to decrease passive release, making the needles ideally suited for an on-demand delivery system.

Fig. 5c depicts the cumulative *in vitro* release profile of insulin from the MoS_2-MN array into PBS (pH 7.4) upon laser irradiation for 10 min with a laser power of 0.5 or 1.0 W cm^{-1} at

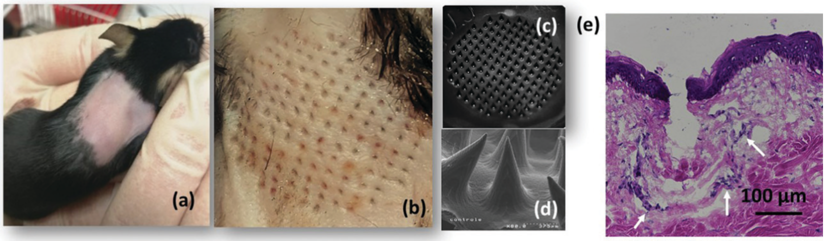

Fig. 4 *In vitro* studies: (a) microscopic images of mouse dorsum shaved before the application of the MoS_2-MN array formed from hydrogel cocktails containing 500 μg mL^{-1} of MoS_2. (b) Image of relevant skin transcutaneously treated with the MoS_2-MN array patch. (c and d) SEM images of the MoS_2-MN array after skin penetration. (e) H&E stained section of the mouse skin penetrated by one MoS_2-MN array patch (white arrows show the infiltration of inflammatory cells).

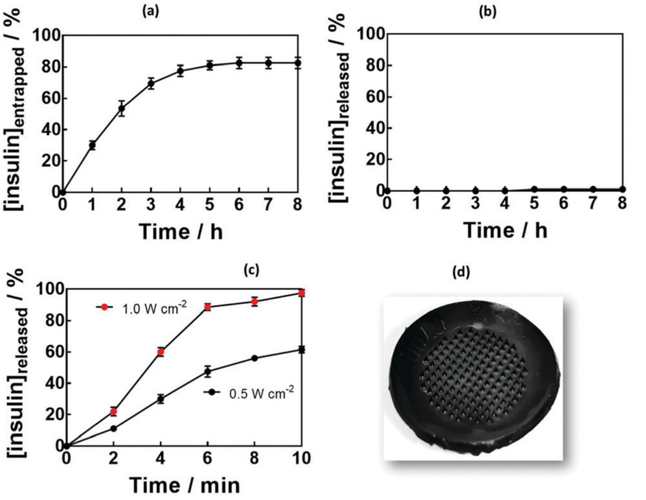

Fig. 5 Insulin entrapment and release behavior of MoS_2-MN patches: (a) entrapment efficiency of human insulin into MoS_2-MNs formed from hydrogel cocktails containing 500 μg mL^{-1} of MoS_2. Loading with insulin was achieved by keeping the MNs at 4 °C for 8 h. An insulin stock solution of 100 μg mL^{-1} was used which corresponds to 100%. (b) Passive cumulative *in vitro* release profile of insulin from the patch into PBS (pH 7.4). (c) Cumulative *in vitro* release profile of insulin from the patch in PBS (pH 7.4) upon the application of different laser power densities at 980 nm, as determined by HPLC: 1.0 W cm^{-2} (red) or 0.5 W cm^{-2} (black) for 10 min. Results are presented as the mean ± standard deviation of four experiments. (d) SEM image of the patch after photothermal release experiments.

980 nm. In a time span of several minutes, up to 100 μg of insulin were released from the patch in a power density-dependent manner.

2.4. *In vitro* pharmacodynamic response of the insulin-loaded MoS_2 MN patch

Fig. 6a exhibits a standard permeation profile of insulin recorded for MoS_2-MN patches loaded with 100 μg of insulin. The high molecular weight and hydrophilic characteristic of insulin restricted passive skin permeation and no skin permeation of insulin was detected without photothermal activation. When mouse skin was subjected to 10 min heating at 0.5 W cm^{-2} (corresponding to a temperature of 50 °C) after a lag time of about 20 min, sustained transdermal transport of insulin occurred over a time period of 2 h. Insulin continues to diffuse through the skin after stopping the NIR stimuli, which indicates that the insulin has passed the stratum corneum and is free to diffuse through the different skin layers. The total amount of permeated insulin after 2 h equals 20.3 ± 2.5 μg, which corresponds to an insulin flux of 10.15 ± 1.25 μg cm^{-2} h^{-1}, superior to the reported flux of 2.0 ± 0.4 μM cm^{-2} h^{-1} by Pillai *et al.* addressing insulin delivery from poloxame-407 gels using transdermal ionophoresis in the presence of menthone as a skin enhancer.[52]

The activity of released insulin was evaluated, *in vitro*, on an immortalized human hepatocyte (IHH) cell line model using native insulin as a positive control and the same culture without insulin as a negative control, as described previously.[53] Fig. 6b indicates that the insulin activity (Akt phosphorylation, p-Akt/Akt ratio) increased when IHH cells were treated with native insulin in comparison to non-treated cells (p-Akt/Akt ratio of 3.7 *versus* 1.0 for the negative control). A comparable p-Akt/Akt ratio of 3.5 was determined on insulin release, indicating that all the activity was preserved under photothermal release from the MoS_2-MN patch.

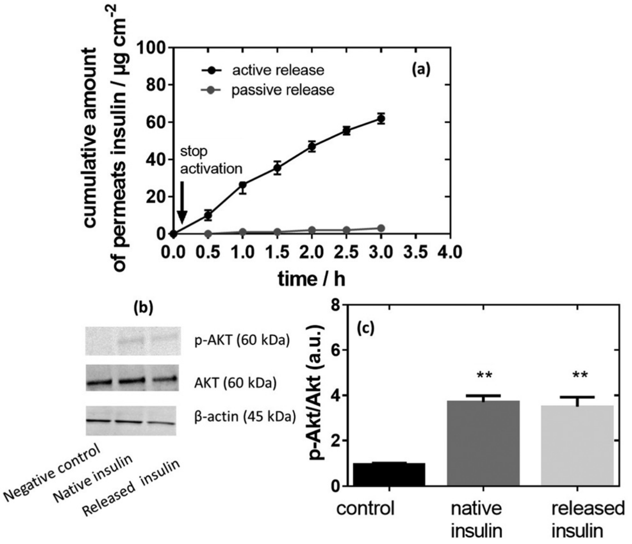

Fig. 6 *In vitro* permeation study: (a) cumulative permeation profile recorded for MoS_2-MN arrays loaded with 100 μg of insulin passive (black) and active (red) upon laser irradiation (980 nm) for 10 min at 0.5 W cm^{-2} (n = 3). Error bars represent means of ± SEM. (b) Insulin activity determined on IHH cells determined *via* western plots of p-Akt/Akt cell lysates from IHH cells incubated under several conditions: without insulin, with native insulin or with photoreleased insulin. (c) Insulin activity shown by the ratio between p-Akt and Akt (A.U.) for all the samples in comparison to a negative control (CTL neg) (cells without insulin treatment). One-way ANOVA and multicomparison test were performed. The results are expressed as mean ± SEM of at least 3 independent samples for each group ($*p < 0.05$, $**p < 0.01$).

2.5. *In vivo* pharmacodynamic response of the insulin-loaded MoS_2 MN array patch

One of the objectives of this work was to test the developed MN array patch in a true preclinical model of diabetes very close to human diabetes, in particular, in terms of insulin need for therapy. Because of their size, diabetic minipigs are the most relevant models available. The efficiency of the insulin-loaded MoS_2 MN array patches was indeed tested on pancreatectomized minipigs. Beforehand, the release of insulin from these patches was tested on mice.

To do so, MoS_2-MN arrays as well as MoS_2-MN arrays loaded with 100 μg mL^{-1} (2.88 insulin units) of insulin were applied on the back of C57BL/6 mice with a homemade applicator and removed after 10 min. The change in blood glucose level (BGL), measured over a period of 3 h after application, is shown in Fig. 7a. Mice treated with a blank MoS_2-MN patch (not loaded with insulin) but activated for 10 min was used as a control. As expected, mice treated with this patch showed no BGL decline even after 3 h. The same was observed for insulin-loaded MoS_2-MN arrays without light activation. Indeed, the

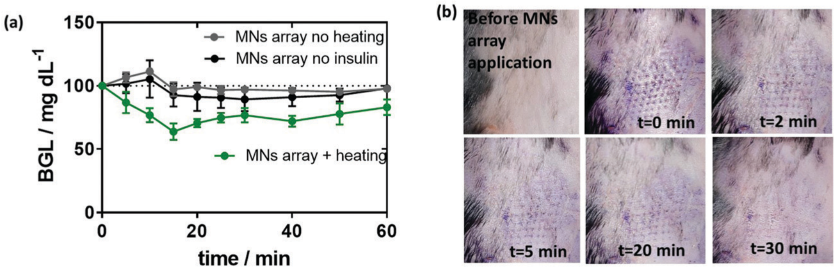

Fig. 7 *In vivo* permeation study in mice: (a) effect of insulin (2.88 IU) loaded onto MoS_2-MN arrays on mouse blood glucose level (BGL) over time: heating: 0.5 W cm^{-2} (10 min, 50 °C). (b) Photographic images of the mouse skin before and after the application of MoS_2-MN arrays.

high molecular weight and hydrophilic characteristics of insulin restricted passive skin permeation. The BGL followed almost the same trend as the blank, indicating that insulin was not released passively. This was different from mice treated with an insulin-loaded MoS_2-MN array photothermally activated for 10 min, where a steady drop in BGL was observed after 15 min, by which it had dropped by 30% from its initial value. These results confirmed that the biological activity of the released insulin remained intact after light exposure.

An important observation was also the time evolution of the marks left by the microneedles on the skin of the treated mice. After 30 min, the marks on the skin have completely faded, indicating that the array did not destroy permanently the skin of the mouse (Fig. 7b).

To complete the results, we took the opportunity of using pancreatectomized Gottingen minipigs as a valuable model of insulin-dependent diabetes.[54] Of particular relevance, diabetic minipigs share many similarities with humans with regard to the pharmacokinetics of compounds after subcutaneous administration, the structure and function of the gastrointestinal tract, the morphology of the pancreas, and the overall metabolic status of the two species.[55,56] Application of a MoS_2-MN array loaded with human insulin on the ear of the minipig resulted in a reduction of the BGL after 30 min from the start of the patch application. The decrease of the BGL coincides with a peak in the plasma insulin concentration, confirming the hypoglycemic effect of insulin released from the patch (Fig. 8a). No visible effects on skin tissue were observed by staining the mini-pig skin with hematoxylin–eosin after the application of the photothermal pulse for 10 min at 0.5 W cm^{-1} corresponding to 50 °C (Fig. 8d).

3. Conclusion

This work demonstrated the first on-demand insulin delivery strategy *via* microneedles using photothermal activation rather than dissolution of microneedles to liberate the cargo. We showed that microneedles formed using molybdenum sulfide (MoS_2) nanosheets loaded onto crosslinked gelatin methacrylate with polyethylene glycol diacrylate represent an appealing platform for on-demand insulin delivery under NIR irradiation. The *in vitro* insulin release profile revealed a remarkable fast release rate, which can be tuned *via* the applied laser light power. The presence of MoS_2 not only helped in improving the mechanical strength and skin penetration capability, but also restricted the passive release of insulin or its burst release. Using mice we first provided the evidence that MoS_2-MNs exhibited excellent glucose regulation in a normal range with a response time of about 15 min, in line with subcutaneous insulin injection. Finally, we confirmed that the MoS_2-MNs patches loaded with insulin have a high potency for reducing glycemia of diabetic mini-pigs, paving the way for developing smart, painless and safe patches for insulin delivery in patients requirring insulin therapy. Also, we do believe that these patches might guide the development of other useful drug delivery platforms. As the polymer is highly crosslinked, no polymer deposit in the skin is likely. Indeed, translational considerations as well as scale-up hurdles will still have to be overcome to consider its

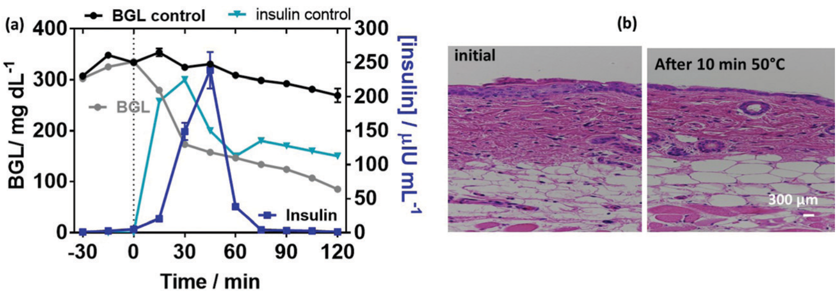

Fig. 8 *In vivo* permeation study in mini-pigs: (a) measurement over time of blood insulin (dark blue line) and blood glucose level (BGL, grey line) in mini-pigs carrying MoS_2-MN array patches loaded with human insulin (1 IU). In a control experiment, insulin was injected subcutaneously (1 IU) and blood insulin (bright blue) and BGL (back) were dosed over time. (b) Hematoxylin and eosin staining showing the histology of the skin after heating for 10 min at 0.5 W cm^{-1} (50 °C).

clinical application in humans in the future. While insulin was used as a model drug here, easy application of this approach to other drugs of interest for on-demand delivery is a goal, *e.g.* pain decreasing drugs. Currently, this technology is based on a portable NIR source and needs to be miniaturized to achieve wearable technology.

4. Experimental section

4.1. Materials

Gelatin, methacrylic anhydride (MA), poly(ethylene glycol) diacrylate (PEGDA, average MW ~ 700 g mol^{-1}), molybdenum(IV) sulfide (MoS_2), phosphate saline buffer (PBS, 1 ×) ethanol (EtOH), 2-hydroxy-4′-(2-hydroxyethoxy)-2-methylpropiophenone (Irgacure 2959), insulin (human recombinant), fluorescein isothiocyanate isomer I (FITC), trifluoroacetic acid (TFA), and FITC-modified insulin were purchased from Sigma-Aldrich. Polydimethylsiloxane (PDMS) (Sylgard® 184) was obtained from Dow Corning Corporation. Acetonitrile was procured from Thermo Fischer Scientific.

4.2. Synthesis of gelatin methacrylate (GelMA)

Methacrylation of gelatin was carried out as described in a previous report with minor modifications.[57] In brief, 10 g of gelatin was added into 100 mL of PBS and heated to 50 °C under constant magnetic stirring. For a 1 : 1 ratio, 10 mL of methacrylic anhydride (MA) was gradually added to the above mixture and the reaction was kept under vigorous stirring for 3 h at 50 °C. The reaction was stopped by adding a five-fold volume (500 mL) of PBS. Residual salts and excess MA were removed by dialysis in distilled water at 40 °C for one week using dialysis tubing with a molecular weight cut-off of 12–14 kDa. Dialysis water was changed twice per day. After lyophilization for one week, GelMA was collected in the form of white porous foam and kept in the dark for further use.

4.3. Preparation of microneedles (MNs)

4.3.1. PDMS mold fabrication. A circular MN array (named C700, diameter 18 mm) was designed with 137 needles of a conical structure and micromachined on an aluminum surface to have a master mold (Fig. S2, ESI†). The needles have the following dimensions: height of 700 μm, length of 400 μm and tip-to-tip distance of 850 μm. This MN array was covered with 10% cross-linked PDMS solution *in vacuo* to remove bubbles and kept at 80 °C for 2 h. The hardened PDMS mold was gently separated from the aluminum master mold.

4.3.2. Microneedle fabrication. Initially, 400 mg of GelMA was dissolved in 1.5 mL of PBS at 65 °C. Then, 10 mg of Irgacure 2959 as a photoinitiator was mixed with 200 mg of PEGDA, 1.0 mg of MoS_2 and 0.2 mL of EtOH. This mixture was sonicated for 8 min. Afterwards, the GelMA solution was mixed with other components and complemented with 2.0 mL of PBS. The final solution was sonicated for another 8 min to remove the possible bubbles and 300 μL of GelMA : PEGDA (20 : 10 weight ratio) mixture was cast into a preheated PDMS mold and kept under back vacuum overnight at 30 °C. UV irradiation (15 cm, 400 W, Delolux 3S) of the PDMS mold for 5 min resulted in the polymerization of the mixture immediately. The formed MNs were gently peeled from the mold, washed for 2 h in PBS to remove any non-polymerized monomers and stored in a desiccator until further use.

4.4. Swelling and degradation experiments

A swelling test of the MNs was performed upon incubation in PBS for 24 h at 32 °C. MNs submerged in PBS were blotted to remove residual liquids, and wet weight (Ww) of the MNs was recorded after MNs reached the equilibrium of swelling. The dry weight (W_d) was measured after complete drying. The swelling ratio was calculated using the formula $[(W_w - W_d)/W_d] \times 100\%$. Three samples were used for the measurements to calculate the mean and standard deviations.

4.5. Characterization and instrumentation

4.5.1. Fourier-transform infrared spectroscopy (FTIR). In the FTIR measurements, a Shimadzu IRAffinity-1 FTIR-ATR spectrometer was used. For each sample, 64 scans were recorded between 4000 and 600 cm^{-1} at a resolution of 4 cm^{-1}.

4.5.2. ^{1}H nuclear magnetic resonance (^{1}H NMR) spectroscopy. ^{1}H NMR spectroscopy was conducted to monitor the methacrylation of gelatin; the spectra were recorded using a Bruker Spectrospin spectrometer operating at 300 MHz and 308 K. Spectral analysis was performed using TopSpin software. To calculate the degree of methacrylation, Internal TMSP was used (0 ppm/integrating for 9 protons) and the methacrylation peaks (5.4–6.0) were integrated for 2 protons. The following equations were applied to calculate the precise amount of methacrylation as mmol methacrylation per g gelatin and also methacrylation percentage.

$$\text{Degree of methacrylation}\left(\frac{\text{mmol}}{\text{g}}\right) = \frac{\int \text{methacryl}}{\int \text{TMSP}} \times \frac{9H}{1H} \times \frac{n(\text{TMSP})[\text{mmol}]}{m(\text{gelatin derivative})[\text{g}]}$$

$$\text{Degree of methacrylation}(\%) = \left(\frac{\int \text{methacryl}}{\int \text{TMSP}} \times \frac{9H}{1H}\right) \times 100$$

4.5.3. Mechanical testing and microscopic analysis. For the determination of the height loss of the MNs after compression with a precise force, a texturometer (TA.XT Plus, Stable Micro Systems) was used. The MN array was placed on the metal platform perpendicularly (tipped up) and correlations between the applied force and deformation of the MNs were recorded. The MN array was pressed at a rate of 0.5 mm s^{-1} from a 20 mm distance and the maximum loading force was set to 45 N.

A digital microscope (VHX 8000, Keyence) was used to observe the morphology (height and width of the base) of the MN array under normal light. MN heights were analyzed before and after 5 s of treatment.

4.5.4. Scanning electron microscopy (SEM). SEM images were obtained using an electron microscope ULTRA 55 (Zeiss, France) equipped with a thermal field emission emitter and three different detectors (an EsB detector with a filter grid, a high-efficiency in-lens SE detector and an Everhart–Thornley secondary electron detector).

4.5.5. Raman spectroscopy. Micro-Raman spectroscopy measurements were performed on a LabRam HR Micro-Raman system (Horiba Jobin Yvon, France) using a 660 nm laser diode as the excitation source. Visible light is focused by a 100× objective. The scattered light is collected by the same objective in backscattering configuration, dispersed with a 1800 mm focal length monochromator and detected using a CCD camera.

4.5.6. Measurement of the photothermal effect. All irradiations were performed in standard 96-well plates. A 980 nm-continuous wave laser (Gbox model, Fournier Medical Solution) was used for the photothermal experiments at a power density of 0.5 W cm^{-2}. This laser was injected into a 400 μm-core fiber and placed at 6 cm from the bottom of the wells. The output was not collimated and the resulting beam divergence allowed uniform illumination up to 4 wells. The temperature changes on the surface of the nanofiber mats were captured with an infrared camera (Thermovision A40) and treated using ThermaCam Researcher Pro 2.9 software.

4.5.7. High-performance liquid chromatography (HPLC) for quantification of insulin. HPLC analysis was performed with a Waters e2695 using a C18 Sunfire™ column (5 μm, 250 × 4.6 mm, Waters Corporation) heated to 30 °C. The mobile phase consists of TFA (0.1%) in water as eluent A and eluent B is TFA (0.1%) in acetonitrile : water (90 : 10%, v/v) (flux: 1 mL min^{-1}). The flux was 85% of A for 20 min and a gradient from 15–35% of B for 15 min, 35–65% for 10 min, then 65% of B for 7 min. A 2789 UV/vis detector (Waters corporation) for 214 nm and a 2475 multi-fluorescence detector (Waters Corporation) for 495/520 nm (excitation/emission) were used.

4.6. Insulin loading and release experiments

4.6.1. Insulin loading. Commercial human insulin was prepared (100 μg mL^{-1}) in PBS and the MN array was immersed in 2.0 mL of insulin solution for 8 h at 4 °C. The concentration of insulin loaded into the MNs was determined by measuring insulin remaining in the solution using HPLC.

4.6.2. Insulin release. Initial release experiments were performed at 37 °C to simulate skin temperature in order to monitor the MN arrays' drug release capability. In this case, MN arrays loaded with insulin were immersed in 2.0 mL of pre-heated PBS and 1.0 mL of the sample was withdrawn after 5 min release intervals by replacing with 1.0 mL of fresh PBS. Samples were analyzed by HPLC.

4.6.3. Photothermal insulin release. Photothermal release experiments were performed in 3.0 mL of phosphate buffered saline (PBS) (pH 7.4). The MNs were irradiated with a continuous wave laser (Gbox model, Fournier Medical Solution, France) with an output light at 980 nm at various power densities (0.5 and 1 W cm^{-2}) for several minutes. The quantity of insulin released was evaluated by HPLC.

4.7. Analysis of the biological activity of the released insulin

The activity of the released insulin was evaluated, *in vitro*, on an immortalized human hepatocyte (IHH) cell line model (Fig. 6b) using native insulin as a positive control and the same culture without insulin as a negative control as described previously.[53] After overnight culture in a serum-free and glucose-free culture medium, IHH cells were incubated for 1 h without insulin (negative control), with native insulin (positive control) and with electrothermally released insulin at a physiological active concentration of 200 nM. After 1 h of incubation, the cells were lysed and proteins were collected. The expression of p-Akt and Akt proteins was evaluated by western blotting analysis. For western blotting experiments, 40 μg of total proteins of each condition was loaded and separated onto a polyacrylamide gel, and then transferred on a nitrocellulose membrane. β-actin was used as an internal control. Immunoblotting for p-Akt and Akt was performed using anti-p-Akt specific antibody (Thr-308, Cell Signaling Technology), anti-Akt specific antibody (sc-8312, Santa Cruz) and fluorescence-coupled secondary antibodies against both mouse and rabbit primary antibodies. Western blot analysis was performed using the Odyssey revelation process and ImageJ quantification technique. A one-way ANOVA test was carried out.

4.8. *In vitro* skin penetration studies

The formed MNs were applied to skin to test their skin penetration ability. Skin permeation studies were performed using fresh mice skin. For this, mice C57BL/6 were anaesthetized with isoflurane, shaved with an electric shaver (Philips Series 7000) and further treated with a depilatory cream (Veet) for 1.5 min. Then the mice were killed by cervical dislocation and the skin from the back of the mice was cut into pieces of at least 20 mm in diameter and preserved in Dulbecco's modified Eagle's medium (DMEM) supplemented with gentamicin (0.4%). The thickness of the skin was determined with a Digimatic micrometer (Mitutoyo) and was 600 ± 5 μm. A specially designed static Franz diffusion cell (Proviscin, France)[51] exhibiting an effective area of 0.78 cm^2 was used for permeability tests. After filling the receptor compartment with degassed PBS (pH = 7.4), the solution was maintained at 32 °C using a circulating bath (Julabo) and stirred with a magnetic stirring bar at around 500 rpm. The mouse skin was carefully clamped between the donor and the receptor compartments (8 mL). Pre-incubation in the receptor compartment medium for 20 min was performed before the MNs were applied to the skin. MNs loaded with 100 μg insulin were used for the permeation studies. The MNs were inserted into the skin gently and a 200 g weight was placed on the microneedle surface for 5 min. After removing the weight, the MN array was left on the skin for another 10 min and then withdrawn. The insertion depth into the skin was determined on frozen tissue sections.

Photothermal activation was performed for 10 min at 980 nm (0.5 W cm^{-2}). At determined time intervals, 300 μL aliquots of diffused solution were removed from the receptor compartment and analyzed using HPLC. After each sampling, an equal volume of fresh diffusion medium was added to the receptor compartment to maintain a constant volume. All experiments were performed in triplicate.

The release and permeation profiles were determined by plotting the cumulative amount of insulin in the receptor compartment (Q_{exp}) against time, $Q_{\text{exp}} = c_n \times V + \sum_{i=1}^{n-1} c_i \times V$, where Q_{exp} is the cumulative amount of insulin diffused through the skin (μg), c_n is the amount of insulin (μg) determined at the nth sampling interval, and V is the volume of the acceptor phase (receptor compartment) (mL). The insulin flux (J) was determined according to $J = A/S$, where J is the flux of insulin through the skin (μg cm^{-2} h^{-1}), A is the linear slope of the cumulative amount *versus* time under equilibrium conditions (μg h^{-1}), and S is the surface of the membrane of the Franz cell (0.78 cm^2). To estimate the amount of insulin trapped in the skin, the skin was added into a water/ice mixture for 10 min and sonicated in the presence of ZnO_2 beads (4 mm in diameter), before being centrifuged for 30 min at 13500 rpm using an ultracentrifuge (Midi Scanfuge ORIGIO). The liquid phase was collected and filtered through a 0.1 μm Nylon filter (Whatman Puradisc 13 mm) and the amount of insulin was determined.

4.9. *In vivo* insulin delivery experiments

4.9.1. Mice model. Delivery of insulin from the MN array was investigated in the C57BL/6 mice model. The day before the experiment, the back of the mouse was shaved (Philips Series 7000). The shaved area was further treated with a depilatory cream (Veet) for 1.5 min to eliminate all the remaining hair. The mice are fasted at the start of the experiment. The blood glucose level was determined using a glucometer. Before the application of the MN patch, the mice were anesthetized with isoflurane for 2 min (level 2, 1 l min^{-1} air). The MN patch loaded with 2.8 IU (100 μg insulin) as well as the control were applied to the shaved area and fixed with the help of adhesive tape (Sparadrap Micropore, 2133). The blood glucose level was determined to define the baseline. The patch was activated for 10 min to reach 50 °C under anesthesia and then removed. The values of blood glucose level determined with a glucometer were plotted against time to obtain the blood glucose level–time profiles. All animal experiments throughout this study were conducted according to the policy of the Federation of European Laboratory Animal Science Association and the European Convention for the Protection of Vertebrate Animals Used for Experimental and Other Scientific Purposes, with the implementation of the principle of 3Rs (replacement, reduction, refinement). The work runs under protocol number APAFIS#20681-2019051614407707v2.

4.9.2. Mini-pigs. Microneedle penetration and insulin delivery *in vivo* were tested on female domestic pigs weighing 52–60 kg. The animals were subjected to total pancreatectomy a day before each experiment. A tunneled central venous catheter into the external jugular vein was placed in each animal facilitating blood sampling. The insulin loaded microneedles (1.0 IU) were placed on the pig's ear and fixed with adhesive tape (Sparadrap Micropore, 2133). The microneedles were activated for 10 min at a temperature of ∼50 °C. Glucose levels were measured directly from fresh blood *via* the central catheter using a commercial glucometer. Blood samples were obtained at different time intervals. Blood samples were centrifuged at 5000 rpm for 10 min at 4 °C and the plasma was immediately separated and stored at −80 °C until analyzed. Radioimmunoassay kits were used for the measurements of insulin (Bi-Insulin RIA®; Bio-Rad, Elexience, Verrières-le-Buisson, France). All the manipulations in pigs, including total pancreatectomy, placing of the catheter, microneedle and patch activation and blood samplings, were performed under general anesthesia with a 2–3% concentration of isoflurane (Aerrane; Baxter, France) and under analgesia with transcutaneous fentanyl (Recuvyra; Elanco; France). Animal studies were approved by the Institutional Ethics Committees for the Care and Use of Experimental Animals of the University of Lille (protocol no. 21080). All experiments were performed in accordance with the guidelines for animal use specified by the European Union Council Directive of September 22, 2010 (2010/63/EU).

Conflicts of interest

There are no conflicts to declare.

Acknowledgements

The Centre National de la Recherche Scientifique (CNRS), the University of Lille, the Hauts-de-France region, and the CPER ''Photonics for Society'' are acknowledged for financial support. BD thanks the Hauts-de-France region for a post-doctoral fellowship. AV thanks the i-SITE foundation of the University of Lille for a PhD fellowship. LR is supported by a CIFRE grant. We acknowledge the help and involvement of the Dhure (Département Hospitalo-Universitaire de Recherche et d'Enseignement) platform in this work related to mini-pigs.

References

1 M. R. Prausnitz and R. Langer, *Nat. Biotechnol.*, 2008, **26**, 1261–1268.

2 V. Georgakilas, J. N. Toiwari, C. Kemp, J. A. Perman, A. B. Boulinos, K. S. Kim and R. Zboril, *Chem. Rev.*, 2016, **9**, 5464–5519.

3 S. Szunerits and R. Boukherroub, *Front. Bioeng. Biotechnol.*, 2018, **6**, 15.

4 X. Jin, D. D. Zhu, B. Z. Chen, M. Ashfaq and X. D. Guo, *Adv. Drug Delivery Rev.*, 2018, **127**, 119–137.

5 S. Chen, H. Matsumoto, Y. Moro-oka, M. Tanaka, Y. Miyahara, T. Suganami and A. Matsumoto, *Adv. Funct. Mater.*, 2018, **29**, 1807369.

6 M. Kirkby, A. R. J. Hutton and R. F. Donnelly, *Pharm. Res.*, 2020, **37**, 117.

7 M. Azmana, S. Mahmood, A. R. Hilles, U. K. Mandal, K. A. S. Saeed Al-Japairai and S. Raman, *J. Drug Delivery Sci. Technol.*, 2020, **60**, 101877.

8 T. Liu, G. Luo, M. Xing, G. L. Tengfei Liu and M. Xing, *Adv. Ther.*, 2020, **3**, 900140.

9 K.-Y. Seong, M.-S. Se, D. Y. Hwang, E. D. O'Cearbhaill, S. Sreenan, J. M. Karp and S. Y. Yang, *J. Controlled Release*, 2017, **265**, 48–56.

10 Y. Zhang, G. Jiang, W. Yu, D. Liu and B. Xu, *Mater. Sci. Eng., C*, 2018, **85**, 18–26.

11 J. Zhuang, F. Rao, D. Wu, Y. Huang, H. Xu, W. Gao, J. Zhang and J. Sun, *Eur. J. Pharm. Biopharm.*, 2020, **157**, 66–73.

12 J. W. Lee, M.-R. Han and J.-H. Park, *J. Drug Targeting*, 2013, **21**, 211–223.

13 S. Kim, H. Yang, J. Eum, Y. Ma, S. F. Lahiji and H. Jung, *Biomaterials*, 2020, **232**, 119733.

14 M.-C. Chen, M.-H. Ling, K.-W. Wang, Z.-W. Lin, B.-H. Lai and D.-H. Chen, *Biomacromolecules*, 2015, **16**, 1598–1607.

15 P. R. Yadav, M. N. Munni, L. Campbell, G. Mostofa, L. Dobson, M. Shittu, S. K. Pattanayek, M. J. Uddin and D. B. Das, *Pharmaceutics*, 2021, **13**, 1132.

16 S. Wang, M. Zhu, L. Zhao, D. Kuang, S. C. Kundu and S. Lu, *ACS Biomater. Sci. Eng.*, 2019, **5**, 1887–1894.

17 M. Zhu, Y. Liu, F. Jiang, J. Cao, S. C. Kundu and S. Lu, *ACS Biomater. Sci. Eng.*, 2020, **6**, 3422–3429.

18 S. Chen, H. Matsumoto, Y. Moro-oka, M. Tanaka, Y. Miyahara, T. Suganami and A. Matsumoto, *ACS Biomater. Sci. Eng.*, 2019, **5**, 5781–5789.

19 Z. Wang, Z. Yang, J. Jiang, Z. Shi, Y. Mao, N. Qin and T. H. Tao, *Adv. Mater.*, 2022, **34**, e2106606.

20 E. M. Migdadi, A. J. Courtenay, I. A. Ismaiel, A. Tekko, M. T. C. McCrudden, M.-C. Kearney, E. McAlister, H. O. McCarthy and R. F. Donnelly, *J. Controlled Release*, 2018, **285**, 142–151.

21 R. F. Donnelly, T. R. R. Singh, M. J. Garland, K. Migalska, R. Majithiya, C. M. McCrudden, P. L. Laxman Kole, T. M. T. Mahmood, H. O. McCarthy and A. D. Woolfson, *Adv. Funct. Mater.*, 2012, **22**, 4879.

22 H. Kim, H. Lee, K.-Y. Seong, E. Lee, S. Y. Yang and J. Yoon, *Adv. Healthcare Mater.*, 2015, **4**, 2071–2077.

23 R. F. Donnelly, C. M. McCrudden, A. Z. Aklkilani, E. Larrañeta, E. McAlister, A. J. Courtenay, M.-C. Kearney, T. R. R. Sing, H. O. McCarthy, V. L. Kett, E. Caffarel-Salvador, S. Al-Zahrani and A. D. Woolfson, *PLoS One*, 2014, **9**, 111547.

24 J. G. Hardy, E. Eneko Larrañeta, R. F. Donnelly, N. McGoldrick, K. Migalska, M. T. C. McCrudden, L. Donnely and C. P. McCoy, *Mol. Pharmaceutics*, 2016, **13**, 907–914.

25 B. Z. Chen, L. Q. Zhang, Y. Y. Xia, X. P. Zhang and X. D. Guo, *Sci. Adv.*, 2020, **6**, eaba7260.

26 S. P. Davis, W. Martanto, M. G. Allen and M. R. Prausnitz, *IEEE Trans. Biomed. Eng.*, 2005, **52**, 909.

27 B. P. Timko, M. Arruebo, S. A. Shankarappa, J. B. McAlvin, O. S. Okonkwo, B. Mizrahi, C. F. Stefanescu, L. Gomez, J. Zhu, A. Zhu, J. Santamaria, R. Langer and D. S. S. Kohane, *Proc. Natl. Acad. Sci. U. S. A.*, 2014, 201322651.

28 H. Peng, Y. Zhou, C. Zhang, M. Wang, S. Zhao, Y. Xu, W. Zhang, H. Xina and X. Wang, *J. Mater. Chem. B*, 2019, **9**, 421–427.

29 T. Liu, G. Jiang, G. Song, J. Zhu and Y. Yang, *Biomed. Microdevices*, 2020, **22**, 12.

30 X. Zhao, Q. Lang, L. Yildirimer, Z. Y. Lin, W. Cui, N. Annabi, K. W. Ng, M. R. Dokmeci, A. M. Ghaemmaghami and A. Khademhosseini, *Adv. Healthcare Mater.*, 2016, **5**, 108–118.

31 M. Sutter, J. H. Siepmann, W. E. Jiskoot and W. Jiskoot, *J. Controlled Release*, 2007, **119**, 301–312.

32 S. S. Chou, B. Kaehr, J. Kim, B. M. Foley, M. De, P. E. Hopkins, J. Huang, C. J. Brinker and V. P. Dravid, *Angew. Chem., Int. Ed.*, 2013, **52**, 4160–4164.

33 W. Yin, J. Yu, F. Lv, L. Yan, L. R. Zheng, Z. Gu and Y. Zhao, *ACS Nano*, 2016, **10**, 11000–11011.

34 C. H. Park, T. Kim, G. H. Lee, K. H. Ku, S.-H. Kim and B. J. Kim, *ACS Appl. Mater. Interfaces*, 2020, **12**, 35415–35423.

35 J.-X. Zhou, L.-N. Tang, F. Yang, F.-X. Liang, H. Wang, Y.-T. Li and G.-J. Zhang, *Analyst*, 2017, **142**, 4322–4329.

36 J.-X. Zhou, F. Ding, L.-N. Tang, T. Li, Y.-H. Li, Y.-J. Zhang, H.-Y. Gong, Y.-T. Li and G.-J. Zhang, *Analyst*, 2018, **143**, 4469–4475.

37 Y. C. Chen, Y. Yang, Y. Xian, P. F. Singh, J. Feng, S. Cui, A. Carrier, K. Oakes, T. Luan and X. Zhang, *ACS Appl. Mater. Interfaces*, 2020, **12**, 352–360.

38 F. M. Koheler, A. Jacobsen, T. Ohn, K. Ensslin and W. J. Stark, *Nanoscale*, 2012, **4**, 3781.

39 I. Altinbasak, R. Jijie, A. Barras, B. Golba, R. Sanyal, J. Bouckaert, D. Drider, R. Bilyy, T. Dumych, S. Paryzhak, V. Vovk, R. Boukherroub, A. Sanyal and S. Szunerits, *ACS Appl. Mater. Interfaces*, 2018, **10**, 41098–41106.

40 D. K. H. Tsang, T. J. Lieberthal, C. Watts, I. E. Dunlop, S. Ramadan, A. E. del Rio Hernandez and N. Klein, *Sci. Rep.*, 2019, **9**, 13946.

41 Y. Oz, A. Barras, R. Sanyal, R. Boukherorub, S. Szunerits and A. Sanyal, *ACS Appl. Mater. Interfaces*, 2017, **9**, 34194–34203.

42 F. Teodorescu, Y. Oz, G. Quéniat, A. Abderrahmani, C. Foulon, M. Lecoeur, R. Sanyal, A. Sanyal, R. Boukherroub and S. Szunerits, *J. Controlled Release*, 2017, **246**, 164–173.

43 M. Xiao, S. Wei, Y. Li, J. Jasensky, J. Chen, C. L. Brooks and Z. Chen, *Chem. Sci.*, 2018, **9**, 1769–1773.

44 Y. Wang, M. Ma, J. Wang, W. Zhang, W. Lu, Y. Gao, B. Zhang and Y. Guo, *Materials*, 2018, **11**, 1345.

45 Y. C. Chen, R. Z. Lin, H. Qi, Y. Yang, H. Bae, J. M. Melero-Martin and A. Khademhosseini, Functional human vascular network generated in photocrosslinkable gelatin methacrylate hydrogels, *Adv. Funct. Mater.*, 2012, **22**, 2027–2039.

46 J. Zhu, X. Zhou, H.-J. Kim, M. Qu, X. Jiang, K. Lee, L. Ren, Q. Wu, C. Wang, X. Zhu, P. Tebon, S. Zhang, J. W. Lee, N. Ashammakhi, S. Ahadian, M. R. Dokmeci, Z. Gu, W. Sun and A. Khademhosseini, *Small*, 2020, **16**, 1905910.

47 Z. Luo, W. Sun, J. Fang, K. Lee, S. Li, Z. Gu, M. R. Dokmeci and A. Khademhosseini, *Adv. Healthcare Mater.*, 2019, **8**, 1801054.

48 X. Chen, N. C. Berner, C. Backes, G. S. Duesberg and A. R. McDonald, *Angew. Chem., Int. Ed.*, 2016, **55**, 5803–5808.

49 R. Ahmad, R. Srivastava, S. Yadav, D. Singh, G. Gupta, S. Chand and S. Sapra, *J. Phys. Chem. Lett.*, 2017, **8**, 1729–1738.

50 H. Amani, M.-A. Shahbazi, C. D'Amico, F. Fontana, S. Abbaszadeh and H. A. Santos, *J. Controlled Release*, 2021, **330**, 185–217.

51 Q. Pagneux, R. Ye, L. Chengnan, A. Barras, N. Hennuyer, B. Staels, D. Caina, J. I. Avila Osses, A. Abderrahmani, V. Plaisance, V. Pawlowski, R. Boukherroub, S. Melinte and S. Szunerits, *Nanoscale Horiz.*, 2020, **5**, 663–670.

52 O. Pillai and R. Panchagnula, *J. Controlled Release*, 2003, **89**, 127.

53 A. Abderrahmani, L. Yengo, R. Caiazzo, M. Canouil, S. Cauchi, V. Raverdy, V. Plaisance, V. Pawlowski, S. Lobbens, J. Maillet, L. Rolland, R. Boutry, G. Queniat, M. Kwapich, M. Tenenbaum, J. Bricambert, S. Saussenthaler, E. Anthony, P. Jha, J. Derop, O. Sand, I. Rabearivelo, A. Leloire, M. Pigeyre, M. Daujat-Chavanieu, S. Gerbal-Chaloin, T. Dayeh, G. Lassailly, P. Mathurin, B. Staels, J. Auwerx, A. Schurmann, C. Postic, C. Schafmayer, J. Hampe, A. Bonnefond, F. Pattou and P. Froguel, *Diabetes*, 2018, **67**, 1310–1321.

54 M. O. Larsen and B. Rolin, *ILAR J.*, 2004, **45**, 303–331.

55 J. Yu, J. Wang, Y. Zhang, G. Chen, W. Mao, Y. Ye, A. R. Kahkoska, J. B. Buse, R. Langer and Z. Gu, *Nat. Biomed. Eng.*, 2020, **4**, 499–506.

56 A. Sterkers, T. Hubert, V. Gmyr, F. Torres, G. Baud, N. Delalleau, M. C. Vantyghem, J. Kerr-Conte, R. Caiazzo and F. Pattou, *Am. J. Transplant.*, 2013, **13**, 891–898.

57 D. Loessner, C. Meinert, E. Kaemmerer, L. C. Martine, K. Yue, P. A. Levett, T. J. Klein, F. P. W. Melchels, A. Khademhosseini and D. W. Hutmache, *Nat. Protoc.*, 2016, **11**, 727–746.